



The Japanese Geotechnical Society

Soils and Foundations

www.sciencedirect.com
journal homepage: www.elsevier.com/locate/sandf



Effect of principal stress axis rotation on cyclic plastic deformation characteristics of unsaturated base course material

Aasim Inam*, Tatsuya Ishikawa, Seiichi Miura

Graduate School of Engineering, Hokkaido University, Japan

Available online 15 June 2012

Abstract

It is generally observed that the stress state induced through traffic loads inside the substructure of pavements cannot be exactly reproduced in laboratory element tests. Moreover, there are not sufficient studies that examine the behavior of granular material under unsaturated conditions, although such conditions are very prevalent in pavement structures. In this research, an attempt is made to determine the cyclic plastic deformation characteristics of unsaturated granular base course material, and to examine the effect of the rotation of the principal stress axis (experienced by pavement elements under traffic loads) on the mechanical behavior of unsaturated granular base course material by applying various loading methods. A series of laboratory element tests using a multi-ring shear apparatus, which can take into account the rotation of the principal stress axis, were carried out on granular base course material under different moisture contents. The experimental results show that the moisture content has an obvious effect on both the shear behavior and the cyclic plastic deformation of granular base course material. However, the moisture content for the maximum deformation of granular base course material varies according to the loading method. It is also explained that cyclic plastic deformation considerably increases due to the rotation of the principal stress axis under repeated axial and shear loading tests. Therefore, the principal stress axis rotation has a significant influence on the cyclic plastic deformation of unsaturated granular base course material.

© 2012 The Japanese Geotechnical Society. Production and hosting by Elsevier B.V. All rights reserved.

Keywords: Base course; Moisture content; Principal stress axis rotation; Multi-ring shear test; Cyclic deformation

1. Introduction

Pavements should transfer traffic loads safely from the top surface to the subgrade soil or bottom layer. There are primarily two types of pavements, namely, flexible and rigid. Flexible pavement structures are typically composed

of a top layer of asphalt concrete, the base course layer consisting of granular material below that, and the subgrade soil or the bottom layer. The main function of the base course layer is to provide structural support to the top layer of the pavement. After the construction of roads, it has been observed that the pavement surface gradually starts to deteriorate. Such deterioration of the pavement causes the loss of its function as a transportation facility. As a result, huge expenditures are incurred for maintenance. One of the reasons for the deterioration of the pavement is the infiltration of water into the base course layer. Throughout the year, this infiltration and seasonal variations in the groundwater level cause a fluctuation in the moisture content inside the base course layer.

*Corresponding author.

E-mail addresses: aasiminam@yahoo.com,
aasiminam@gmail.com (A. Inam).

Peer review under responsibility of The Japanese Geotechnical Society.



Accordingly, it is pertinent to mention that unsaturated behavior is more prevalent in the base course layer.

Besides the significance of understanding the behavior of the unsaturated granular base course layer, an appropriate loading method for laboratory element tests is also critical for pavement design and analysis. It is noted in various research works that the behavior of pavement structures under traffic loads differs from that in repeated axial loading tests. The main difference is due to the rotation of the principal stress axis. The importance of the effect of the principal stress axis rotation, which is frequently encountered under *in situ* conditions, on the deformation behavior of coarse grained soil, has been pointed out by Miura et al. (1986). The rotation of the principal stress axis, experienced by an element of pavements subjected to traffic loads, is indicated in Fig. 1, which was redrawn from Lekarp et al. (2000a) and is also explained by Powrie et al. (2007). This phenomenon is produced under traffic loads, as vehicles approach and then pass a given location along the pavement. The outcome of laboratory element tests, in which principal stress axis rotation is applied, represents more reliable deformation behavior of granular material, and its importance to the performance of pavements and railroad tracks has been mentioned by various researchers (Chan and Brown, 1994; Brown, 1996; Gräbe and Clayton, 2009). Numerous studies have been carried out to analyze the influence of principal stress axis rotation; however, the effect of principal stress axis rotation on the plastic deformation is not yet fully understood (Lekarp et al., 2000b). In addition, laboratory element tests, such as triaxial compression tests, generally employ axial compression loading without principal stress axis rotation. Consequently, the phenomenon of principal stress axis rotation has not been reproduced concisely through conventional testing methods.

Keeping the aforementioned in mind, Ishikawa et al. (2007) developed a multi-ring shear apparatus for laboratory element tests. The multi-ring shear apparatus can take into account the rotation of the principal stress axis, like *in situ* conditions under moving-wheel loads, and is used to evaluate the strength–deformation characteristics of granular base course material. Furthermore, the performance of the multi-ring shear apparatus was evaluated by comparing the test results with those of hollow cylinder torsional shear tests. It was revealed that the results obtained from the static shearing multi-ring shear tests

are approximately similar to the stress–strain relationship and the internal friction angle of those obtained from hollow cylinder torsional shear tests performed under similar experimental conditions for various granular materials. In all the previous research works, the multi-ring shear apparatus was employed to evaluate the mechanical behavior of saturated and air-dried granular materials. Accordingly, the mechanical behavior of saturated and air-dried granular base course materials is quite well understood and at an advanced level. However, the number of studies that examines the mechanical response of granular base course material under unsaturated conditions is not sufficient. In this research, an attempt is made to examine the effect of principal stress axis rotation on the cyclic plastic deformation behavior of unsaturated granular base course material under different moisture contents with the multi-ring shear apparatus. In this regard, the internal friction angle and the rotation of the principal stress axis are also evaluated.

2. Test material

2.1. Physical properties

C-40 (Crusher-run which has a maximum particle size of 40 mm) is used in Japanese roads as the base course material; it is composed of angular, crushed, hard andesite stone. The grading of C-40 means it has a grain size distribution between 0 and 40 mm. In the multi-ring shear apparatus, the width of the sample is 60 mm. In this research, the maximum particle size selected was 9.5 mm, because according to standard specifications for transportation materials and methods of sampling and testing by AASHTO T 307-99 (2007), mold sizes used to fabricate specimens of the minimum diameter, equal to five times the maximum particle size, are selected. Therefore, in this research, C-9.5 (Crusher-run which has a maximum particle size of 9.5 mm) material was selected for the multi-ring shear tests, which is about one-fourth the mean particle size of the original C-40. C-9.5 material is prepared by screening out particles larger than 9.5 mm from the C-40 material and washing the inside of a 0.075-mm sieve. The process of washing the inside of the sieve was carried out in order to remove the fine particles, because fine particles can enter between the small gaps of the rings of the multi-ring shear apparatus. After washing the sieve, the

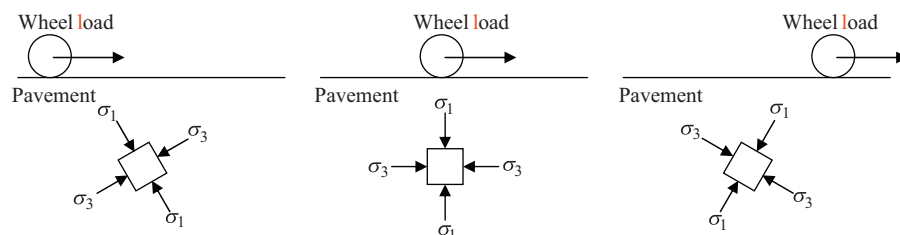


Fig. 1. Rotation of principal stress axis beneath wheel load (Revision of Lekarp et al., 2000a).

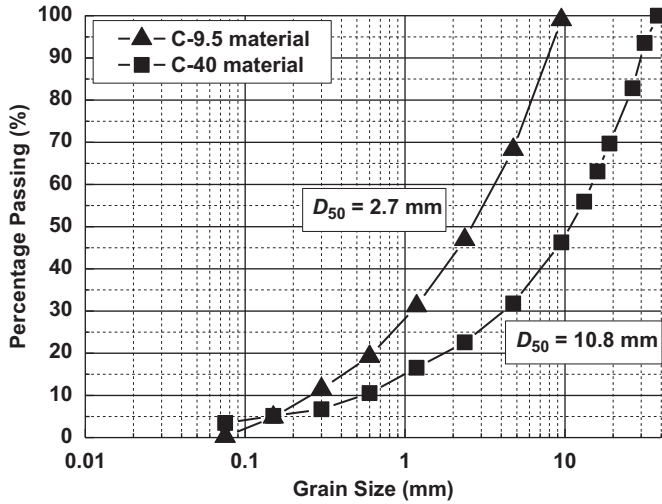


Fig. 2. Particle size distribution curves for test materials.

Table 1
Physical properties of test materials.

Name of material	Coefficient of uniformity, U_c	Average diameter, D_{50} (mm)	Specific gravity, G_s
C-9.5	13.9	2.7	2.675
C-40	27.3	10.8	2.720

C-9.5 material is dried in an oven for at least 24 h. Particle size distribution curves for the C-9.5 and the C-40 materials are shown in Fig. 2. The physical properties of C-9.5 and C-40 are described in Table 1.

2.2. Moisture–density relationship

The compaction curve for the C-9.5 material was determined by the A-b method of the Japanese Industrial Standard (Japanese Standards Association, 2009). In this method, a mold diameter of 100 mm, a mold height of 127 mm and a drop height of 300 mm for the rammer are used. The C-9.5 material is compacted in three equal layers by applying 25 blows to each layer with a 2.5-kg rammer. The moisture–density curve, with an optimum moisture content of $w_{opt}=9.5\%$ and a maximum dry density of $\rho_{dmax}=1.775\text{ g/cm}^3$, is obtained as shown in Fig. 3.

2.3. Soil–water characteristic curve

In accordance with the standards by the Japanese Geotechnical Society (2009), water retentivity tests on the C-9.5 material were carried out using a medium-size triaxial apparatus to determine the soil–water characteristic curve (SWCC) of the unsaturated soils. Moreover, the outcome of the water retentivity tests can also be applied to determine the internal friction angle of the unsaturated specimen. The apparatus can control pore air pressure u_a and pore water pressure u_w at the cap and the pedestal,

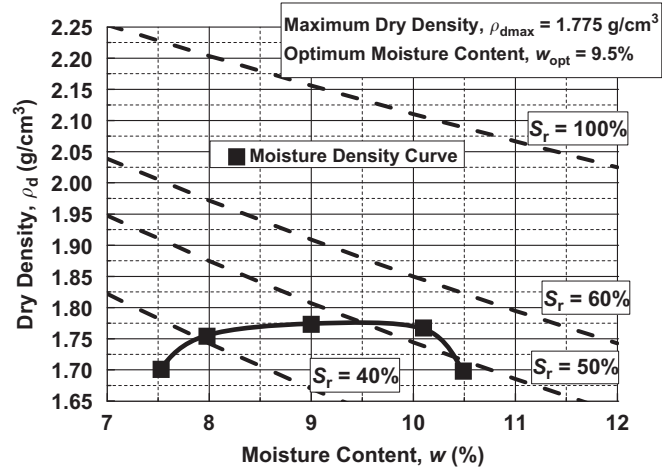


Fig. 3. Moisture–density curve.

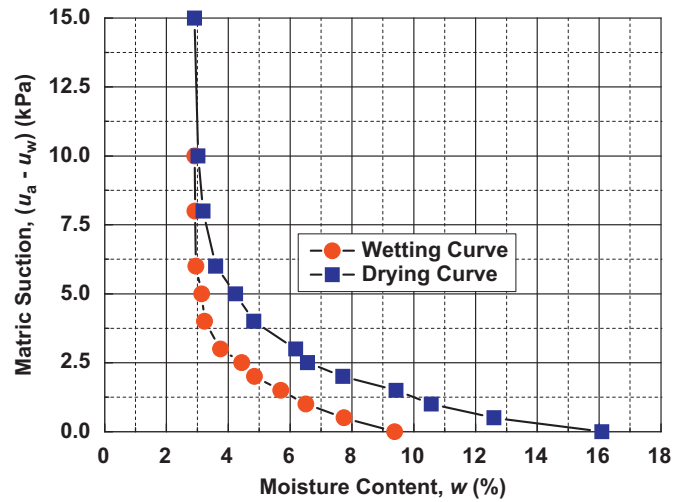


Fig. 4. Soil–water characteristic curves.

separately. Pore water pressure is applied through a hydrophilic versapore membrane filter, and pore air pressure is applied through a hydrophobic polyflon filter to the cylindrical specimen (300 mm in height and 150 mm in diameter). The C-9.5 material was prepared in the triaxial apparatus so that the dry density after consolidation became 1.580 g/cm^3 , which was the same dry density as that used before conducting the multi-ring shear tests in this research. After setting the specimen in the triaxial cell, de-aired water is permeated into the specimen until the degree of saturation reaches 85% or more. After isotropic consolidation (confining pressure of $\sigma_c=249\text{ kPa}$, $u_a=200\text{ kPa}$ and $u_w=200\text{ kPa}$), the pore water pressure is gradually decreased to obtain an unsaturated specimen, while maintaining a confining pressure of 249 kPa and a pore air pressure of 200 kPa. After the completion of the drying process, the wetting process is started to illustrate the matric suction value at a certain moisture content. Fig. 4 shows the results of the water retentivity tests on the C-9.5 material. In the wetting process of SWCC, the suction

value decreases in comparison to the suction value for the drying curve at the same moisture content. As a result of the decrease in suction value, Fig. 4 shows the hysteresis between the wetting and the drying curves of SWCC. One of the reasons for the hysteresis is that it takes a long time to complete the drying process and, as a result, diffused air appears under the versapore membrane during the wetting process. Based on the above reason, the drying curve, which is considered to be more accurate than the wetting curve, has been selected for the calculation of the internal friction angle in this research. In Fig. 4, the drying curve shows that residual moisture content w is about 2.92%, which is equivalent to 11.3% of the residual degree of saturation S_{r0} .

3. Testing method

3.1. Multi-ring shear apparatus

A schematic diagram of the multi-ring shear apparatus is shown in Fig. 5. It mainly consists of a bottom plate, a loading plate and rigid rings. The specimen is placed over the bottom plate and is confined by outer and inner rigid rings. Each ring has a height of 20 mm. The inside surface of the outer rings and the outside surface of the inner rings were designed in such a way that the friction between the specimen and the rings is reduced to the extent where each ring can move freely during loading.

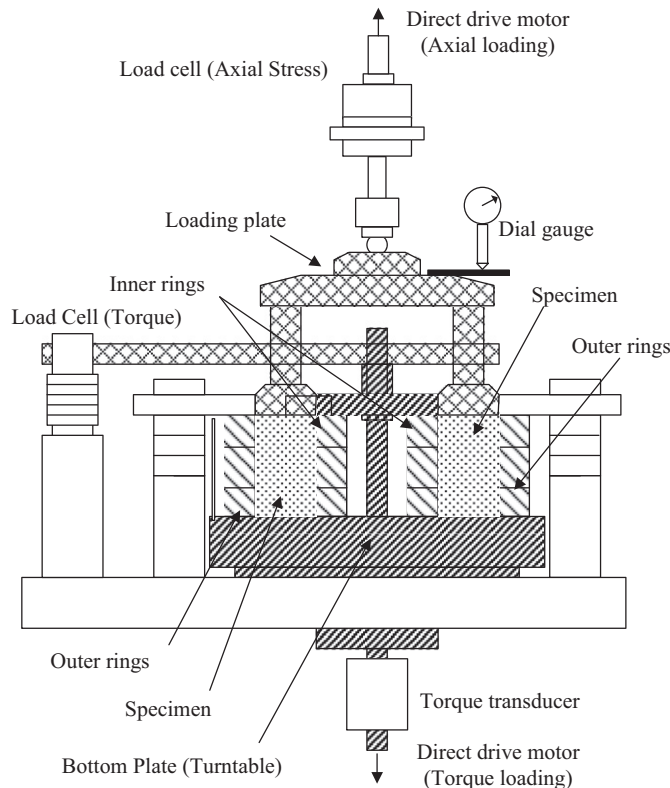


Fig. 5. Schematic diagram of multi-ring shear apparatus.

Torque loading is applied through the direct drive motor placed below the bottom plate (turntable), while the loading plate remains fixed. Shear stress $\tau_{a\theta}$ is measured with a torque transducer installed under the bottom plate and a load cell for the torque mounted on the loading plate. Shear strain $\gamma_{a\theta}$ is calculated from the rotational angle of the direct drive motor for the torque loading and the vertical displacement by an external displacement transducer (dial gage). Axial loading is also applied to the specimen through the direct drive motor attached to the loading plate. Axial stress σ_a is measured with a load cell mounted on the loading plate, and axial strain ϵ_a is measured by an external displacement transducer (dial gage). The axial strain is also considered as the volumetric strain ϵ_v of the specimen, as radial strain ϵ_r and circumferential strain ϵ_θ are zero in the multi-ring shear tests. The size, load, stress and strain, used in the multi-ring shear tests, are defined in Fig. 6. The width of the specimen is 60 mm (120 mm inside diameter and 240 mm outside diameter) and the height is 60 mm.

3.2. Experimental conditions

A series of static and cyclic loading tests were performed with the multi-ring shear apparatus. The moisture content of the specimen was selected on the basis of the field data obtained from the Tomakomai field measuring site near Sapporo, Japan. The field data show that the degree of saturation S_r of the C-40 base course material lies in the range of 20–50% throughout the year. It was also observed that during the multi-ring shear tests, water can penetrate to the lower part of the specimen at a higher degree of saturation. This may result in the non-uniformity of the specimen. Keeping the field data in mind, and in order to minimize the non-uniformity of the water, moisture

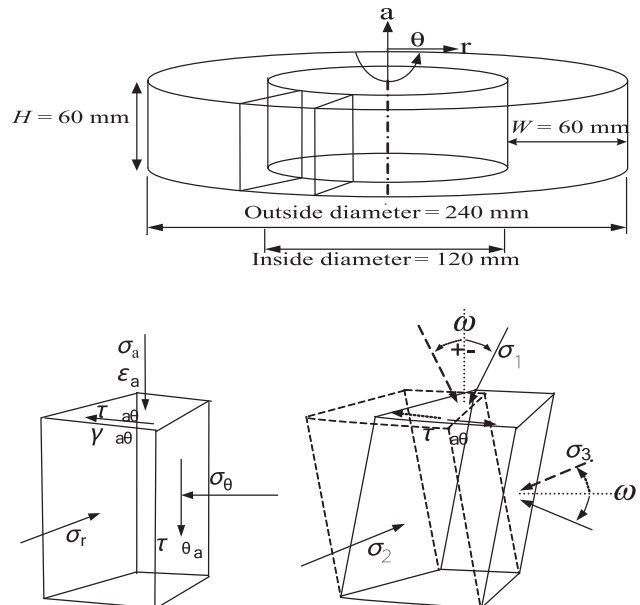


Fig. 6. Definitions for stress and deformation.

contents of $w=5\%$ ($S_r=19.3\%$), 9% ($S_r=34.8\%$) and 13% ($S_r=50.2\%$) were selected for the unsaturated specimens. The prescribed moisture content is added to the oven-dried C-9.5 material. An oven-dried sample was also selected to compare the results with those of the unsaturated specimen. Afterwards, the C-9.5 material is placed in three equal layers over the bottom plate, confined by outer and inner rigid rings, and compacted uniformly to achieve the desired dry density. In accordance with Japanese highway standards, a maximum dry density of 95% is commonly taken in field conditions. However, due to the limitation of the multi-ring shear apparatus, 95% of the maximum dry density could not be achieved; therefore, a dry density of $1.581\text{--}1.583\text{ g/cm}^3$ was selected for the multi-ring shear tests, which is about 89% of the maximum dry density ($\rho_{dmax}=1.775\text{ g/cm}^3$).

The loading conditions for the multi-ring shear tests were determined based on a stress analysis of a Japanese paved road model by GAMES (General Analysis Multi Layered Elastic Systems, Maina and Matsui, 2004). In this regard, a Japanese paved road model under standard design wheel loads is selected, as shown in Fig. 7. It was redrawn from Ishikawa et al. (2008). The properties of the pavement layers, which include elastic coefficient E and Poisson's ratio ν , the standard wheel load, the wheel diameter and the distance between wheels, shown in Fig. 7, are also indicated in the Pavement Design Manual

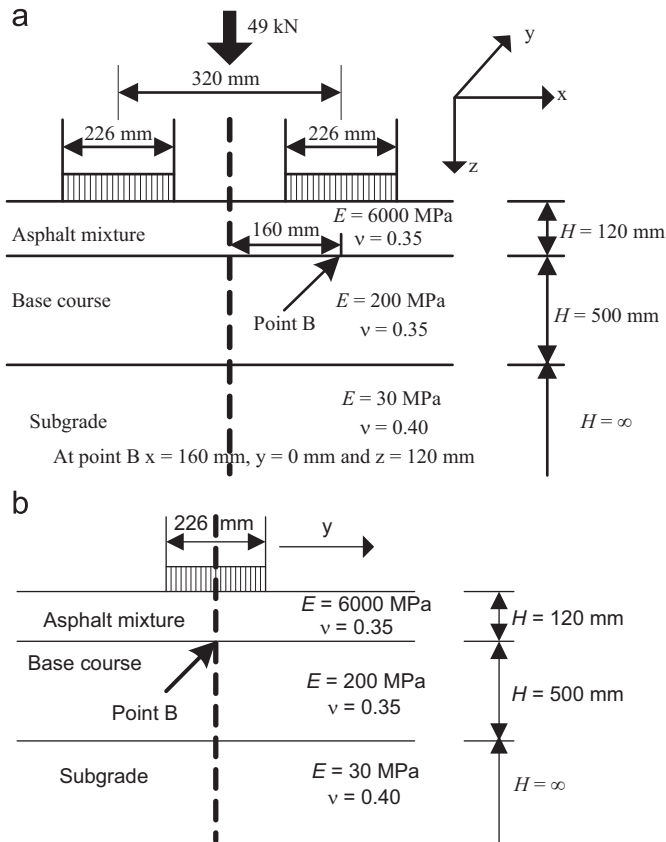


Fig. 7. Model for stress analysis. (a) Cross section and (b) longitudinal section.

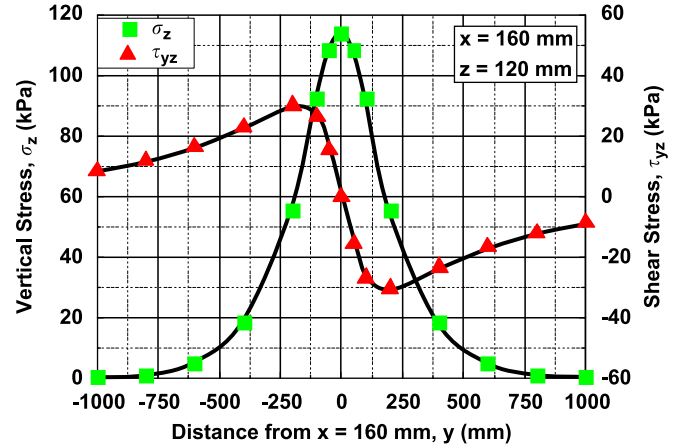


Fig. 8. Vertical and shear stress distributions.

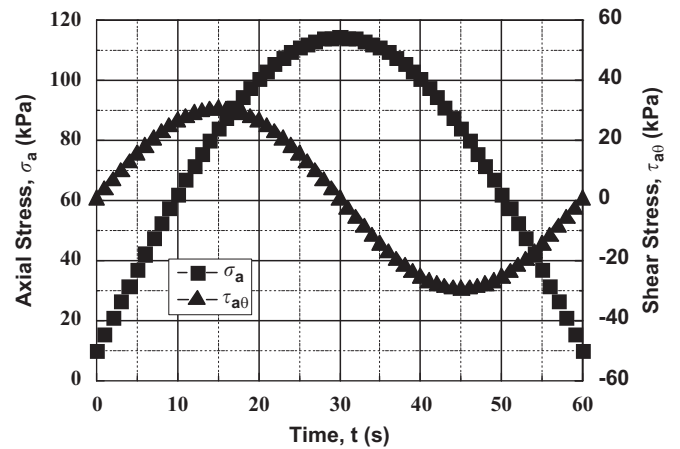


Fig. 9. Cyclic loading pattern in multi-ring shear tests.

for Japanese paved roads issued by the Japanese Road Association (2006). The standard design wheel load of 49 kN was applied to find the stress distribution under the moving-wheel load at Point B in Fig. 7. Fig. 8 shows the vertical stress σ_z and the shear stress τ_{yz} distributions obtained from the stress analysis. On the basis of the stress analysis under the moving-wheel load, the maximum vertical stress at Point B was 114.2 kPa , while the shear stress was 0 kPa at the same coordinates. The shear stress reached the maximum value of $\pm 30\text{ kPa}$ at $x=160\text{ mm}$, $y=\pm 200\text{ mm}$ and $z=120\text{ mm}$ as the vehicle approached and passed Point B, as shown in Fig. 8.

The multi-ring shear apparatus simulates the field loading conditions by applying the axial load and the shear load in a sinusoidal waveform, as shown in Fig. 9. Fig. 9 indicates the same maximum axial stress and shear stress values as those obtained through the stress analysis under the standard design wheel load of 49 kN . The sinusoidal waveform, shown in Fig. 9, is reasonably similar to the stress sequence produced through the moving-wheel loads under actual field conditions. A loading frequency of 0.02 Hz for the cyclic loading tests was adopted due to the limitation of the multi-ring shear apparatus. Another

reason for adopting the lower loading frequency was to provide the appropriate time for the plastic deformation response during cyclic loading in the multi-ring shear tests.

After preparing the sample, static and cyclic loading tests were performed on the C-9.5 material to examine the mechanical behavior of the base course material under different moisture contents using the multi-ring shear apparatus. In the case of the static tests, shear stress $\tau_{a\theta}$ was monotonically increased at the rate of a shear strain of $\gamma_{a\theta}=0.1\%/min$, while keeping axial stress σ_a constant.

In the cyclic loading tests, two loading modes were implemented to evaluate the cyclic deformation characteristics of the unsaturated specimen. One mode is the cyclic axial loading mode, which is considered as repeated axial loading without rotation of the principal stress axis. In this method, only the axial load in the sinusoidal waveform is cyclically applied to the specimen and maximum axial stress σ_{amax} is taken as 114.2 kPa. Hereafter, in this research, the cyclic axial tests without principal stress axis rotation will be referred to as repeated axial loading tests. The other mode is the cyclic axial and shear loading mode, in which the axial load and the shear load, both in the sinusoidal waveform, are cyclically applied to the specimen. The shear load is cyclically applied for bidirectional loading, similar to two-way traffic on pavement, by changing the phase angle of 180° for every succeeding loading cycle. The shear stress distribution, in the form of the sinusoidal waveform for one-way traffic and two-way traffic, is elaborated in Fig. 10. This test is considered as repeated axial and shear loading, in which the rotation of the principal stress axis occurs similarly to *in situ* traffic loading conditions. In repeated axial and shear loading tests, two types of loading conditions were applied. For one loading condition, the maximum axial stress of $\sigma_{amax}=114.2$ kPa and the maximum shear stress of $\tau_{a\theta max}=30$ kPa were considered, as shown in Fig. 9. For the other loading condition, the maximum axial stress of 114.2 kPa and the maximum shear stress of 15 kPa were adopted to further analyze the behavior of the principal stress axis rotation under different moisture contents. The

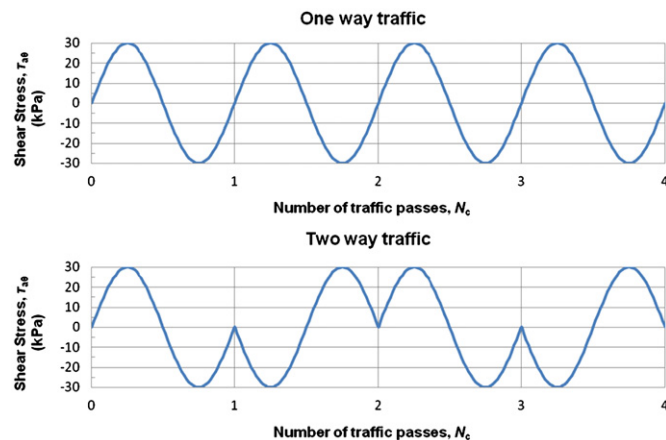


Fig. 10. Shear stress distribution for one-way and two-way traffic.

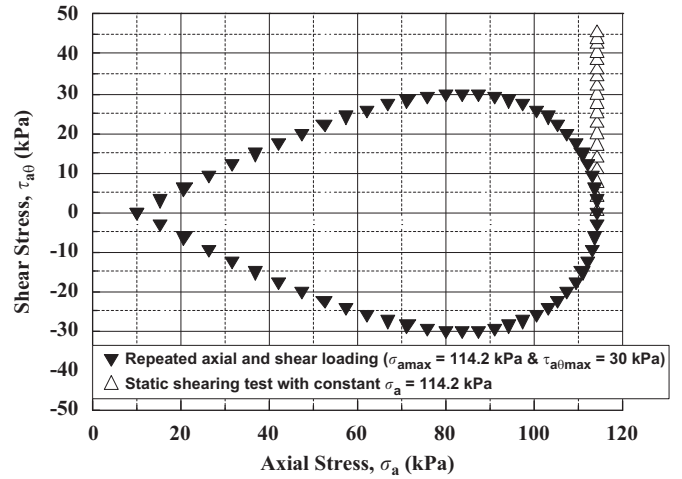


Fig. 11. σ_a - $\tau_{a\theta}$ relationships for static shearing and repeated axial and shear loading.

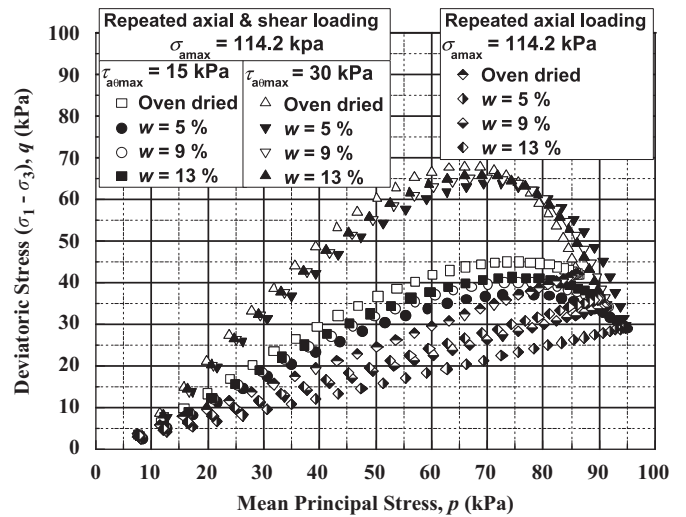


Fig. 12. Stress paths for cyclic loading tests.

axial stress and the shear stress relationships for the static shearing tests and the repeated axial and shear loading tests ($\tau_{a\theta max}=30$ kPa) are shown in Fig. 11. The stress paths between mean principal stress $p=(\sigma_1+\sigma_2+\sigma_3)/3$ and deviatoric stress $q=(\sigma_1-\sigma_3)$ for cyclic loading under different moisture contents are shown in Fig. 12. The principal stress values of σ_1 , σ_2 and σ_3 for the cyclic loading tests were calculated through Eqs. (5), (6) and (7), which are described in a latter section. Keeping in mind the foregoing, the experimental conditions for the multi-ring shear tests performed in this research are summarized in Table 2.

4. Results and discussions

4.1. Influence of moisture content on shear behavior

The results of the static shearing tests are presented in Figs. 13–19. They show the relationships among shear strain $\gamma_{a\theta}$, shear stress $\tau_{a\theta}$ and axial strain ϵ_a under different

Table 2
Experimental conditions for multi-ring shear tests.

Static shearing tests			
Moisture content	Initial dry density, ρ_{d0}	Dry density after consolidation, ρ_{dc}	Constant axial stress, σ_a
(%)	(g/cm ³)	(g/cm ³)	(kPa)
Oven dried	1.560	1.581	114.2
5	1.560	1.581	114.2
9	1.560	1.581	114.2
13	1.560	1.581	114.2

Repeated axial loading tests				
Moisture content, w	Dry density before test, ρ_{d0}	Axial stress, σ_{amax}	Loading frequency,	Number of loading cycles, N_c
(%)	(g/cm ³)	(kPa)	(Hz)	
Oven dried	1.583	114.2	0.02	400
5	1.582	114.2	0.02	400
9	1.583	114.2	0.02	400
13	1.582	114.2	0.02	400

Repeated axial and shear loading tests					
Moisture content, w	Dry density before test, ρ_{d0}	Axial stress, σ_{amax}	Shear stress, τ_{a0max}	Loading frequency	Number of loading cycles, N_c
(%)	(g/cm ³)	(kPa)	(kPa)	(Hz)	
Oven dried	1.581	114.2	30	0.02	400
5	1.582	114.2	30	0.02	400
9	1.581	114.2	30	0.02	400
13	1.582	114.2	30	0.02	400
Oven dried	1.581	114.2	15	0.02	400
5	1.581	114.2	15	0.02	400
9	1.581	114.2	15	0.02	400
13	1.582	114.2	15	0.02	400

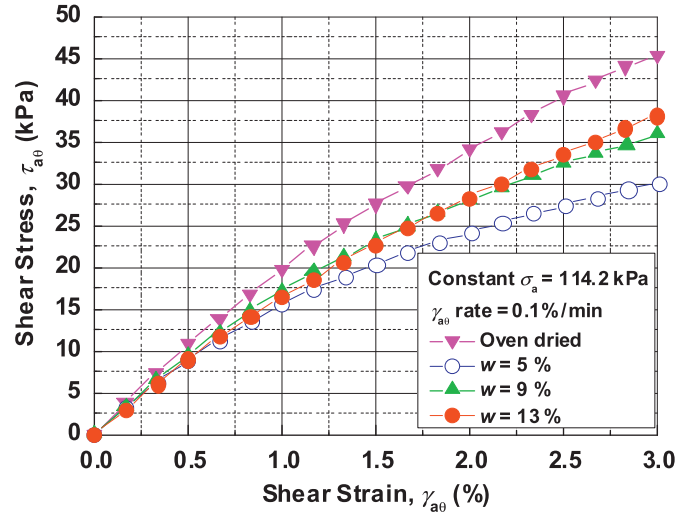


Fig. 14. γ_{a0} - τ_{a0} relationships in static shearing tests.

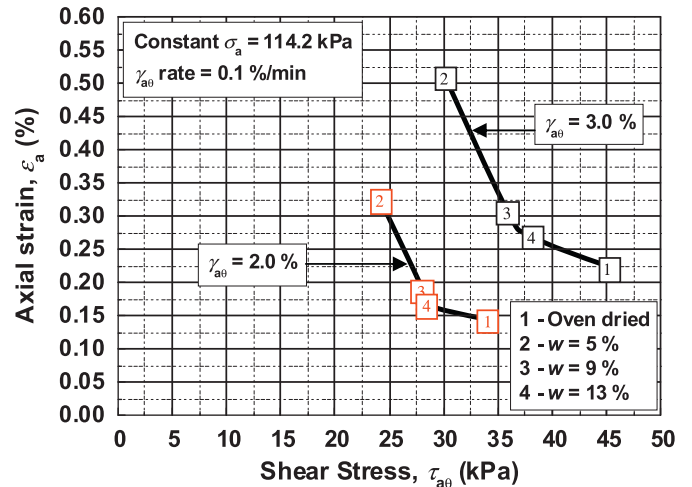


Fig. 15. τ_{a0} - ϵ_a relationships during static shearing tests at same shear strain.

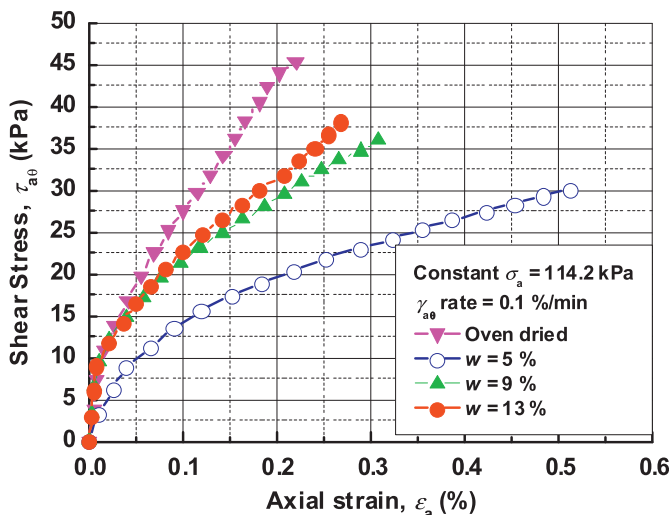


Fig. 13. ϵ_a - τ_{a0} relationships in static shearing tests.

moisture contents. Figs. 13 and 14 clearly show that an increase in the shear stress on each curve causes an increase in the axial strain and the shear strain on the same curve. However, when comparing any two curves obtained from the static shearing tests under different moisture contents, the following trends can be seen as general shear behavior, as shown in Figs. 15–17.

- Shear stress is inversely proportional to axial strain at the same shear strain.
- Shear stress is directly proportional to shear strain at the same axial strain.
- Shear strain is directly proportional to axial strain at the same shear stress.

On the basis of Fig. 8, the shear behavior of the granular base course material was analyzed under an axial stress of

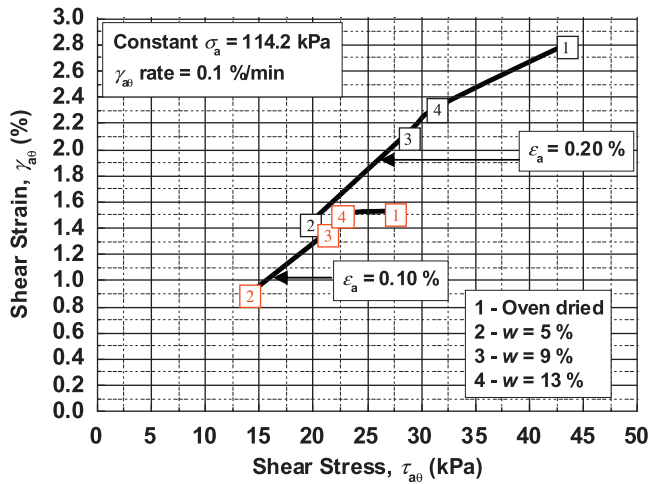


Fig. 16. τ_{a0} - γ_{a0} relationships during static shearing tests at same axial strain.

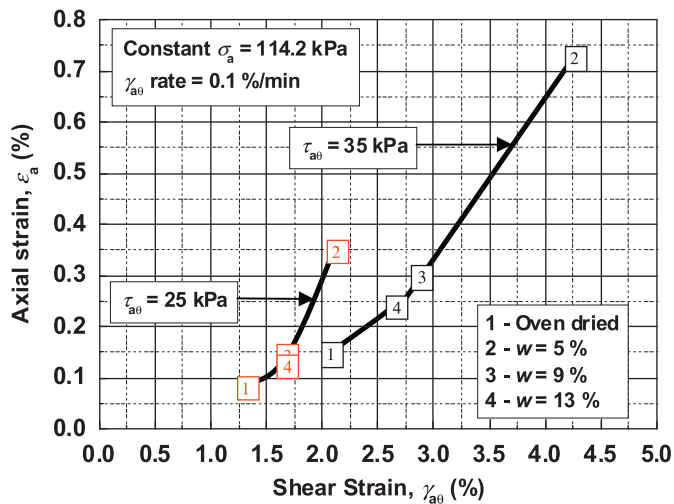


Fig. 17. γ_{a0} - ϵ_a relationships during static shearing tests at same shear stress.

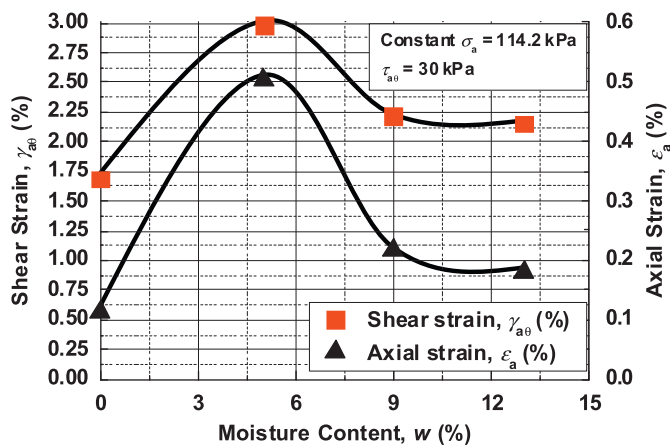


Fig. 18. w - γ_{a0} and w - ϵ_a relationships in static shearing tests.

114.2 kPa and a shear stress of 30 kPa at different moisture contents. In this regard, Fig. 18 shows the relationships between moisture content-shear strain and moisture

content-axial strain at the shear stress of 30 kPa. It is further elaborated that the oven-dried sample has the minimum shear strain and axial strain at the shear stress of 30 kPa. The graph also shows that the sample with a 5% moisture content has the maximum shear strain and axial strain at the shear stress of 30 kPa. The decreasing sequence of axial strain and shear strain, under the constant shear stress of 30 kPa, is 5% moisture content, 9% moisture content, 13% moisture content and finally oven-dried.

During static shearing tests, shear loading was applied up to a shear strain of 3%. A shear strain of 3% was taken due to the limitation of the torque transducer installed in the multi-ring shear apparatus. On this basis, the shear stress and the axial strain behavior were analyzed under different moisture contents at the shear strain of 3%, as shown in Fig. 19. It is seen that the oven-dried sample has the minimum axial strain and the maximum shear stress at the shear strain of 3%. On the other hand, the sample with a 5% moisture content has the maximum axial strain and the minimum shear stress at the shear strain of 3%. The sequence for the increase in shear stress and the decrease in axial strain at the shear strain of 3% under different moisture contents is the same as that mentioned in the above paragraph. The shear stress values at the shear strain of 3%, for all the specimens mentioned in Fig. 19, are applied to calculate the internal friction angle, as these values are considered to be the ultimate shear stress in this research.

A sieve analysis was carried out before and after each static shearing test. Fig. 20 shows an example of the particle size distribution curves before and after testing. It was found that there is no breakage of the particles or changes in the particle size distribution before or after testing.

4.2. Influence of moisture content on internal friction angle

In order to understand the dependency of the shear behavior of the base course material on the moisture

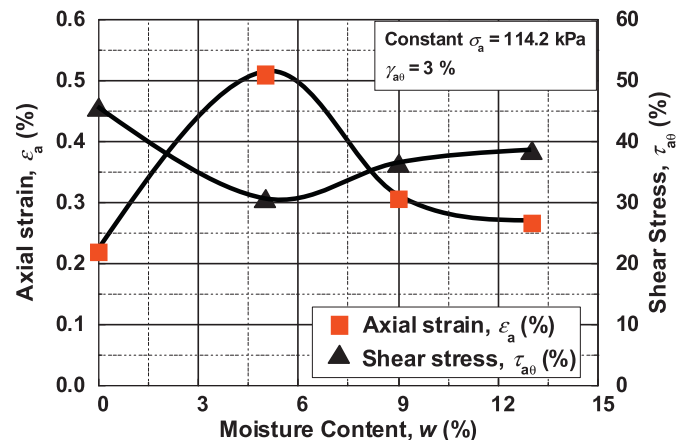


Fig. 19. w - ϵ_a and w - τ_{a0} relationships in static shearing tests.

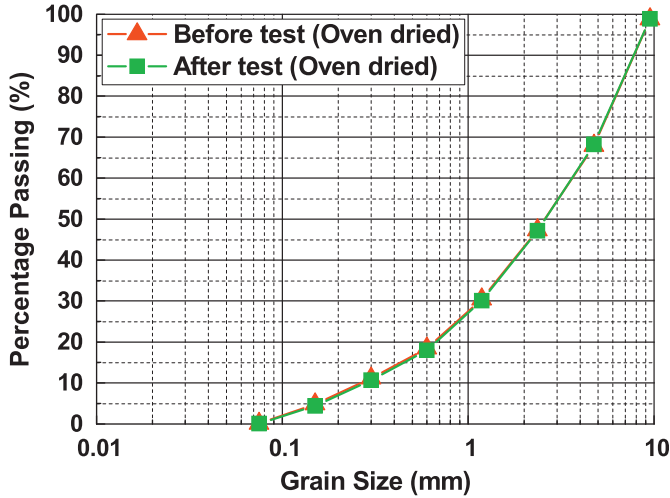


Fig. 20. Particle size distribution curves before and after static shearing tests.

content, the internal friction angle is calculated by applying the shear strength equations for unsaturated soils, as mentioned in Eqs. (1)–(3).

$$\sigma' = (\sigma_a - u_a) + \chi(u_a - u_w) \tag{1}$$

(Bishop’s equation for unsaturated soils)

$$\chi = \frac{S_r - S_{r0}}{1 - S_{r0}} \tag{2}$$

(Vanpalli and Fredlund, 1999; Lu and Likos, 2004)

$$\tau = c' + \sigma' \tan \phi' \tag{3}$$

(Coulomb’s equation)

where τ : shear stress value at the shear strain of 3%, c' : effective cohesion, σ' : effective normal stress, σ_a : axial stress, u_a : pore air pressure, u_w : pore water pressure, $(\sigma_a - u_a)$: net normal stress, ϕ' : effective internal friction angle, $(u_a - u_w)$: matric suction, χ : parameter related to the degree of saturation of the soil, S_r : degree of saturation at any matric suction and S_{r0} : residual degree of saturation.

The difference between the pore air pressure and the pore water pressure acting on the contractile skin is defined as the matric suction (Fredlund and Rahardjo, 1993). It is further explained that the air–water interface in the unsaturated soil is called the contractile skin, which possesses a property called surface tension. As a result of surface tension in the contractile skin, the capillary effect appears in the unsaturated soil. It is found that due to this capillary effect, the water pressure in the capillary height is negative and the air pressure is atmospheric, which constitutes matric suction $(u_a - u_w)$. The second part of Bishop’s equation for unsaturated soil (Eq. (1)) illustrates suction stress $\chi(u_a - u_w)$, which is mainly dependent on the degree of saturation and the matric suction value. Bishop’s equation for unsaturated soil (Eq. (1)) describes the effect of suction stress on the effective normal stress. Due to the increase in suction stress, the effective normal stress

increases and, as a result, the shear stress increases. Matric suction values were obtained from the soil–water characteristic curve in which a dry density of 1.580 g/cm^3 , after consolidation, was maintained throughout the water retentivity tests, as shown in Fig. 4. In the case of the static shearing tests, the initial dry density was set at 1.581 g/cm^3 . However, the dry density after the static shearing tests, at the shear strain of 3%, slightly increases due to a small increase in axial strain, as shown in Fig. 19. Based on the small axial strain occurrence, and as a result of the slight increase in dry density, the matric suction values obtained from the soil–water characteristic curve shown in Fig. 4 are considered appropriate for the multi-ring shear tests. During the multi-ring shear tests on the unsaturated C-9.5 material, the pore air pressure is thought to remain at atmospheric pressure, while the pore water pressure becomes negative, as shown in Fig. 4. Andrew et al. (2004) explained that no true cohesion occurs in granular material without cementation, as was also reported by other researchers. Therefore, in this research, effective cohesion c' is assumed to be zero.

Based on the above discussion, effective internal friction angle ϕ' , under different moisture contents, is calculated as shown in Table 3. In soil mechanics, the effective internal friction angle is generally calculated at the peak shear stress of the soil. In this research, however, the effective internal friction angle is calculated at 3% of the shear strain. The shear stress of the C-9.5 material, at the shear strain of 3% (ultimate shear stress in this study), is quite a bit less than the peak shear stress of the C-9.5 material. Therefore, the values for the internal friction angles mentioned in Table 3 are comparatively lower than the values generally used for crusher-run materials at the peak shear stress. The results show that four different effective internal friction angles are derived from the same material with different moisture contents. The effective internal friction angle for the specimen with the moisture content of 5% has the minimum value, while the angle for the oven-dried specimen has the maximum value. One of the reasons for the four different effective internal friction

Table 3
Calculation of internal friction angle.

No.	Moisture content, w (%)	Degree of saturation, S_r (%)	χ	Shear stress at shear strain of 3%, τ (kPa)	Matric suction, $(u_a - u_w)$ (kPa)	Effective internal friction angle, ϕ' (deg.)
1	Oven dried	0	0	45.2	0	21.6
2	5	19.3	0.1	30.1	3.8	14.7
3	9	34.8	0.3	35.9	1.7	17.4
4	13	50.2	0.4	38.1	0.4	18.4

Residual degree of saturation, $S_{r0}=11.30\%$ (value obtained from SWCC curve); Axial stress, $\sigma_a=114.2 \text{ kPa}$; Pore air pressure, $u_a=0 \text{ kPa}$; Effective cohesion, $c'=0 \text{ kPa}$.

angles being derived from the same material is that the effective internal friction angle is not calculated at the peak shear stress of the C-9.5 material. Secondly, the C-9.5 material with varied moisture states can have different shear stress values under the shear strain of 3%, which is far from the peak shear stress. The same behavior was experienced by Ishikawa et al. (2008), namely, that at a shear strain of 3%, saturated gravel and air-dried gravel achieved different shear stress values. In order to understand the shear behavior of the C-9.5 material, Bishop's equation for unsaturated soils is analyzed. In light of Eq. (3), the shear strength of the C-9.5 material is mainly dependent on four factors, namely, the effective cohesion, the net normal stress, the matric suction and the effective internal friction angle.

On the basis of previous researches, e.g., Andrew et al. (2004), the effective cohesion is assumed to be zero. The net normal stress is the same for all specimens of the C-9.5 material. The matric suction, after being multiplied by the χ parameter, has an insignificant influence on the shear behavior of the C-9.5 material. This is because the capillary effect in the C-9.5 material is not dominant enough to cause suction stress to develop. Therefore, the shear strength of the C-9.5 material is greatly dependent on the internal friction angle. The only factor which can influence the internal friction angle is the moisture content. It is found that, with the addition of the moisture content to the oven-dried sample, the shear strength of the samples with moisture contents of 5, 9 and 13% are less when compared with the oven-dried sample. When samples with moisture contents of 5, 9 and 13% are compared, the results show that the sample with the moisture content of 5% has the minimum shear strength. One of the reasons for this behavior is the non-existence of apparent cohesion at a lower degree of saturation; and therefore, the shear strength of the sample with the moisture content of 5% decreases. The other reason could be that the testing samples are under exhausted and undrained conditions. Therefore, before the tests, the sample with the moisture content of 5% has more air voids and a lower moisture content compared to the samples with moisture contents of 9 and 13%. Therefore, the sample with the moisture content of 5% has a greater tendency for a decrease in air void and, as a result, the shear strength decreases for the sample with the moisture content of 5%. In light of the above discussion, and according to Table 3, moisture content influences the shear behavior and, as a result, the effective internal friction angle varies under different moisture contents. The influence of the moisture content on the deformation behavior in multi-ring shear tests under different loading methods will be explained in detail in latter sections of this research.

4.3. Deformation behavior under cyclic loading

In the case of a pavement analysis, permanent axial strain is an important factor in assessing the failure or the

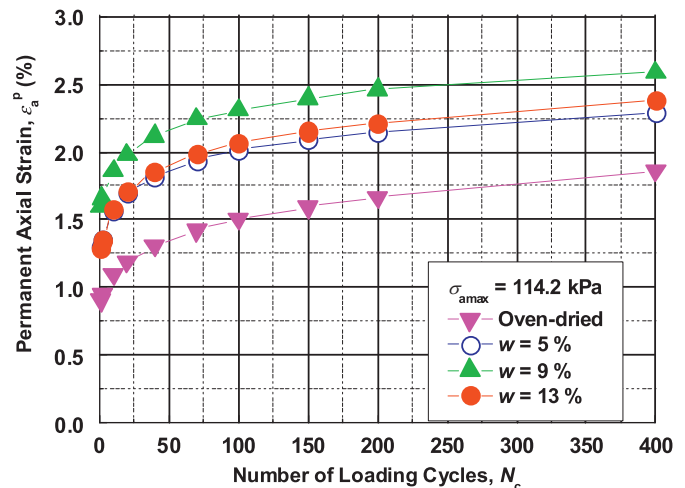


Fig. 21. Permanent deformation during repeated axial loading tests.

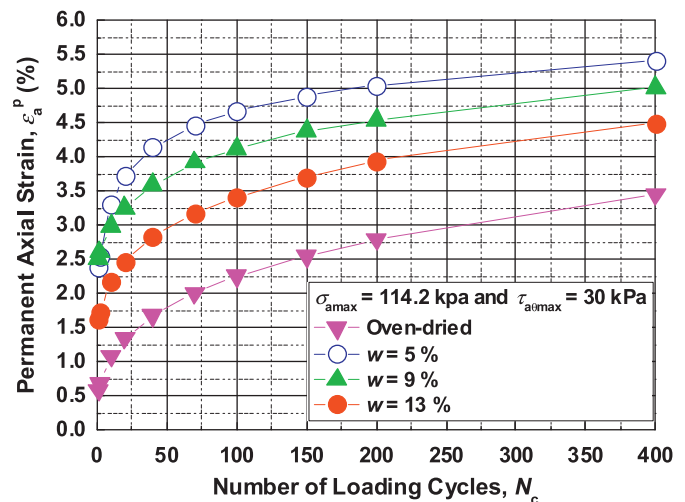


Fig. 22. Permanent deformation during repeated axial and shear loading tests.

deterioration of pavements. It is also noticed that rutting, which is one of the critical distresses in pavements, may occur due to permanent axial strain. Therefore, it is valuable to analyze the cyclic plastic deformation behavior with and without principal stress axis rotation under different moisture contents. The outcome of cyclic loading tests for unsaturated specimens are presented in Figs. 21 and 22 in the form of cumulative permanent axial strain ϵ_a^p at different numbers of loading cycles N_c . Permanent axial strain represents irrecoverable deformation. Figs. 21 and 22 show that, with an increasing number of loading cycles, the permanent deformation increases considerably during the initial stage of loading. Similar behavior is observed in field data on roads, namely, that the most significant permanent deformation occurs during the first or second year of service life (Khogali and Elhoussein, 2004), the granular material subsequently starts to stabilize and permanent deformation curves become flatter.

4.4. Influence of moisture content on deformation behavior

The permanent axial deformation of the base course material specimen may be influenced by several factors, namely, physical characteristics such as the particle size distribution, density achieved before the application of loading, the magnitude and the type of loading and the moisture content.

The particle size distribution of the C-9.5 material is examined before and after each test, and there is no breakage of particles or changes in the particle size distribution regardless of the moisture content. The same dry densities were taken for all the specimens before the tests and the same magnitude of loading for each type was applied, as mentioned in Table 2. Accordingly, when comparing the cumulative permanent axial strain under the same loading conditions, the moisture content is the only variable which influences the mechanical response of the C-9.5 material under cyclic loading with and without principal stress axis rotation.

Fig. 23 shows the axial strain behavior of unsaturated specimens under different types of loading methods. The influence of the moisture content on the cumulative permanent axial strain behavior for repeated axial loading and repeated axial and shear loading tests is evaluated at the 400th loading cycle. Fig. 23 shows that the oven-dried sample in the repeated axial loading tests has a minimum cumulative permanent axial strain ϵ_a^p . This reveals that the oven-dried sample has the slightest change in height, and accordingly, the minimum rearrangement of particles occurs. Subsequently, the increase in moisture content causes an increase in cumulative permanent axial strain until the moisture content reaches 9%; and therefore, the settlement of the particles also increases. With further increases in the moisture content, up to 13%, the

cumulative permanent axial strain drops and the deformation of sample decreases.

In Fig. 23, when comparing the cumulative permanent axial strain of the unsaturated samples under repeated axial and shear loading tests ($\tau_{a\theta\max} = 30$ kPa), it is found that the oven-dried sample has the minimum cumulative permanent axial strain, resulting in the smallest change in the height of the specimen. Fig. 23 shows that with an increase in moisture content, up to 6%, the cumulative permanent axial strain increases significantly and reaches the maximum cumulative permanent axial strain ϵ_a^p . With further increases in the moisture content, up to 13%, the cumulative permanent axial strain decreases gradually and the settlement of the sample decreases.

In order to assess the influence of the moisture content on the cumulative permanent axial strain, another repeated axial and shear loading test ($\tau_{a\theta\max} = 15$ kPa) was conducted. Fig. 23 illustrates that the influence of the moisture content on the cumulative permanent axial strain, due to the repeated axial and shear loading tests ($\tau_{a\theta\max} = 15$ kPa), is similar to the above-discussed behavior. However, in the repeated axial and shear loading tests ($\tau_{a\theta\max} = 15$ kPa), the maximum cumulative permanent axial strain occurred at the moisture content of about 8%, which falls within the other two cyclic loading test results previously mentioned.

As mentioned above, a similar trend was observed in the static shearing tests. They show that the maximum axial deformation occurs at the moisture content of 5%, which is in proximity to the repeated axial and shear loading tests ($\tau_{a\theta\max} = 30$ kPa), as shown in Fig. 23.

The above discussion elucidates that, as a result of adding moisture content to the oven-dried material in the ascending order mentioned in Table 2, air voids decrease for the testing specimen. In the process of the increase in moisture content, and consequently, the decrease in air voids of the testing specimen, the moisture content reaches a certain point where the maximum cumulative permanent axial strain occurs. After that point, the cumulative permanent axial strain gradually decreases. However, in Fig. 23, the peak of the each curve reaches a different moisture content. This shows that the influence of the moisture content, when obtaining the maximum cumulative permanent axial strain, is greatly dependent on the loading method.

Based on the above discussion, it is revealed that the influence of the moisture content on the deformation behavior is similar for all loading methods, but that the differences lie in the magnitude of the deformation and that the maximum cumulative permanent axial strain occurs at different moisture contents and under various loading methods. These differences will be further explained in the following sections.

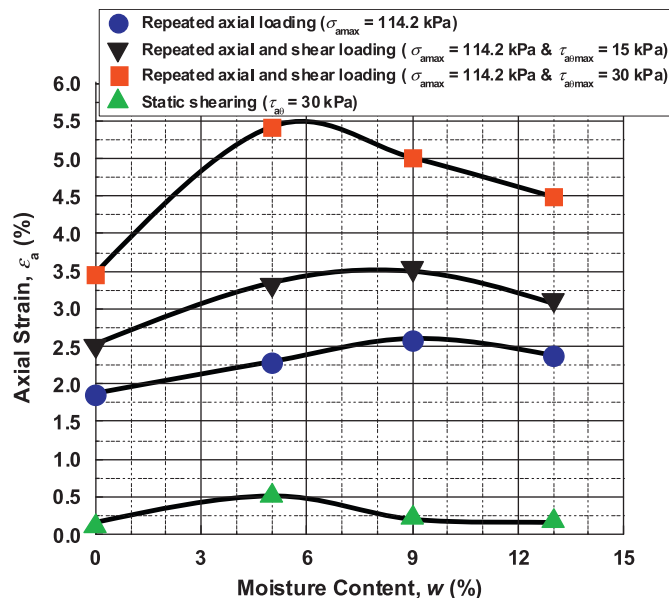


Fig. 23. Moisture content–axial strain relationships.

4.5. Calculation of rotational angle of principal stress axis

The rotational angle of principal stress axis ω is calculated to evaluate the general stress conditions of the

C-9.5 material due to the repeated axial and shear loading tests under different moisture contents. The rotational angle of the principal stress axis, major principal stress σ_1 , intermediate principal stress σ_2 , minor principal stress σ_3 and coefficient of earth pressure at rest K_0 can be calculated with the following equations:

Rotational angle of principal stress axis,

$$\omega = \sin^{-1} \sqrt{\frac{\sigma_2 - \sigma_3}{\sigma_1 - \sigma_3}} \quad (4)$$

Major principal stress,

$$\sigma_1 = \frac{\sigma_a + K_0 \sigma_a}{2} + \frac{\sqrt{(\sigma_a - K_0 \sigma_a)^2 + 4\tau_{a\theta}^2}}{2} \quad (5)$$

Intermediate principal stress,

$$\sigma_2 = \sigma_r = K_0 \sigma_a \quad (6)$$

Minor principal stress,

$$\sigma_3 = \frac{\sigma_a + K_0 \sigma_a}{2} - \frac{\sqrt{(\sigma_a - K_0 \sigma_a)^2 + 4\tau_{a\theta}^2}}{2} \quad (7)$$

Coefficient of earth pressure at rest,

$$K_0 = 1 - \sin \phi' \text{ (Jáky's formula)} \quad (8)$$

The principal stresses and the rotational angle of the principal stress axis have been calculated by inserting the values of the coefficient of earth pressure K , the cyclic axial stress values and the cyclic shear stress values for the repeated axial and shear loading tests into Eqs. (4)–(7). The rotational angle of the principal stress axis is mainly dependent on the axial stress, the shear stress and the coefficient of earth pressure. As already described in this research, a shear strain of 3%, obtained from the static shearing tests, is considered when calculating the effective internal friction angles. The effective internal friction angles obtained from the static shearing multi-ring shear tests at a shear strain of 3%, as mentioned in Table 3, are inserted into Eq. (8) to determine the coefficient of earth pressure. Keeping in mind the ultimate shear stress of 3% of the shear strain, to calculate the effective internal friction angle, the K value for the C-9.5 material obtained from Jáky's formula is higher, in comparison to the K_0 values generally considered for coarse grained granular material. It is assumed that Jáky's formula is applicable to the C-9.5 material, because there are few research works on the estimation method of K_0 for coarse granular material. During cyclic loading tests, the coefficient of earth pressure may change with the number of loading cycles for each test. In this research, lateral stress σ_r was not measured. For this reason, the coefficient of earth pressure is assumed to be constant throughout the tests. In view of the above explanation, the purpose of this calculation is to analyze the effect of the cyclic shear stress and the coefficient of earth pressure at different saturation states on the rotational angle of the principal stress axis under the same cyclic axial stress. The other purpose is to evaluate the effect of the maximum

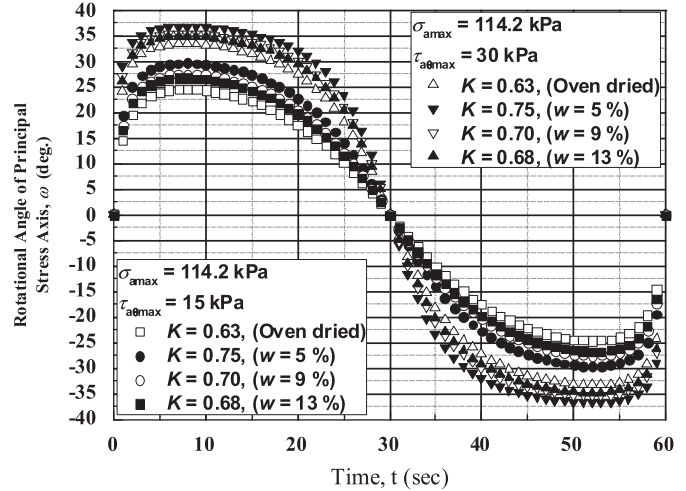


Fig. 24. Rotational angle of principal stress axis in repeated axial and shear loading tests.

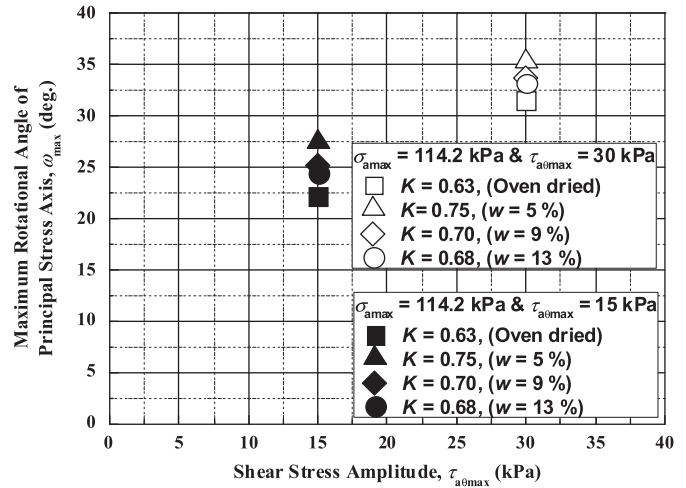


Fig. 25. $\tau_{a\theta\max}$ - ω_{\max} relationships in repeated axial and shear loading tests.

shear stress under the repeated axial and shear loading tests on the relationship between the maximum cumulative permanent axial strain and the maximum rotational angle of principal stress axis ω_{\max} at different saturation states.

Fig. 24 shows that changes in the rotational angle of the principal stress axis during a loading cycle of repeated axial and shear loading tests ($\tau_{a\theta\max} = 30$ kPa) and ($\tau_{a\theta\max} = 15$ kPa) under different saturation states. The rotational angle of the principal stress axis increases cyclically and reaches the highest value at a certain combination of axial and shear stresses. In other words, the maximum rotational angle of the principal stress axis is mainly dependent on the loading conditions of the multi-ring shear tests. The graph also elucidates that the maximum rotational angle of the principal stress axis for the repeated axial and shear loading tests ($\tau_{a\theta\max} = 30$ kPa) and ($\tau_{a\theta\max} = 15$ kPa) occurs after the same interval of time. The sign for the rotational angle of the principal stress axis

changes continuously from positive to negative as the shear stress cyclically changes from positive to negative and *vice versa*.

In Fig. 25, the relationship between shear stress amplitude $\tau_{a\theta\max}$ and the maximum rotational angle of principal stress axis ω_{\max} at the coefficient of earth pressure for different saturation states is elaborated. It shows that the higher the shear stress amplitude is, the larger the rotational angle of principal stress axis becomes under a constant coefficient of earth pressure. Similarly, the higher the coefficient of earth pressure is, the larger the rotational angle of the principal stress axis becomes under a constant shear stress amplitude. The results explain that the variation in maximum rotational angles of the principal stress axis, due to changes in the coefficient of earth pressure from 0.63 to 0.75 at the same shear stress amplitude, is smaller compared to the variation in maximum rotational angles of the principal stress axis due to changes in the shear stress amplitude from 15 to 30 kPa under the same coefficient of earth pressure.

In this research, an attempt is also made to analyze the effect of the maximum rotational angle of principal stress axis ω_{\max} on the maximum cumulative permanent axial strain $e_{a\max}^p$ obtained from each test under repeated axial and shear loading tests. The same coefficient of earth pressure, as that assumed above, is taken for the analysis. Fig. 26 shows that the maximum rotational angle of the principal stress axis depends on the coefficient of earth pressure and the shear stress amplitude to influence the maximum permanent axial strain values. It is observed that the rotational angle of the principal stress axis increases with increases in the coefficient of earth pressure and the shear stress amplitude and, as a result, the cumulative permanent axial strain also increases under the same cyclic axial stress. However, in Fig. 26, at the shear stress amplitude of 15 kPa, the sample with the moisture content of 9% has a lower coefficient of earth pressure compared to the sample with the moisture content of 5%, but the

sample with the moisture content of 9%, has more permanent axial strain and a smaller maximum rotational angle of the principal stress axis. This contradiction is due to the assumption of the coefficient of earth pressure, which does not reflect the actual state of the sample at the maximum cumulative permanent axial strain. Therefore, it is necessary to investigate the coefficient of earth pressure values during cyclic loading multi-ring shear tests in order to confirm the effect of the rotational angle of the principal stress axis on the cyclic plastic deformation behavior.

Fig. 27 shows an example of the relationships between the mean principal stress and the rotational angle of the principal stress axis during cyclic loading tests for the oven dried samples. During a loading cycle, the mean principal stress under each loading method has the same value at the same interval of time. However, the rotational angle of the principal stress axis varies under each loading method during a loading cycle at the same interval of time. One point must be kept in mind, namely, that the loading cycle of the axial stress is the same for all types of cyclic loading tests employed in this research, but only the shear stress amplitude changes in the cyclic loading tests. Therefore, due to the shift from one type of cyclic loading test to the other type of cyclic loading test, the major and the minor principal stresses also vary due to changes in the shear stress amplitude at the same coefficient of earth pressure. It is found that when the shear stress amplitude increases from 15 to 30 kPa, increases in the major principal stresses occur equally to the decrease in minor principal stresses and that no deviation occurs in the intermediate principal stresses during a loading cycle at the same coefficient of earth pressure. This reveals that the mean principal stresses remain the same for all the loading methods under the same coefficient of earth pressure. However, deviations in the major and the minor principal stresses, due to changes in the shear stress amplitude, cause an alteration in the rotational angle of the principal stress axis. It is also indicated in Fig. 27 that when the shear stress amplitude

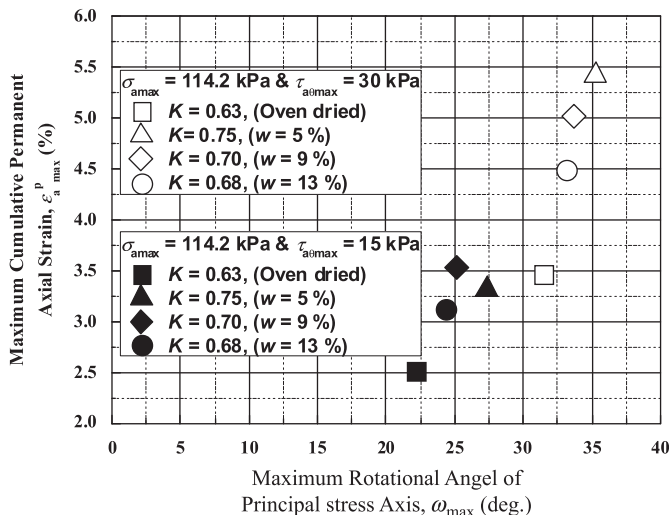


Fig. 26. ω_{\max} – $e_{a\max}^p$ relationships in repeated axial and shear loading tests.

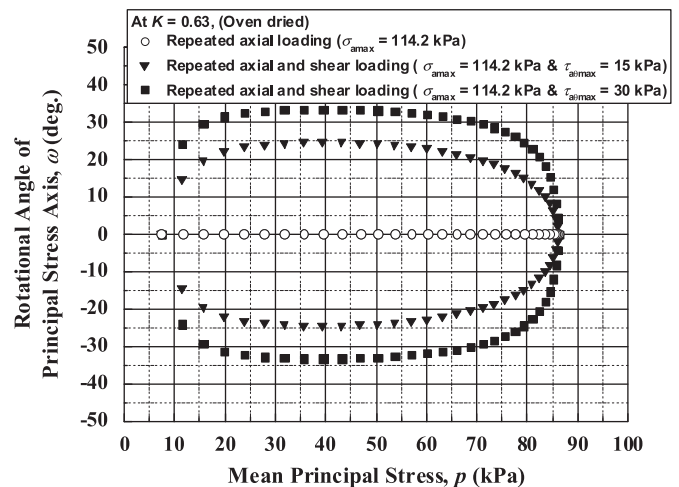


Fig. 27. p – ω relationships during a loading cycle of cyclic loading tests.

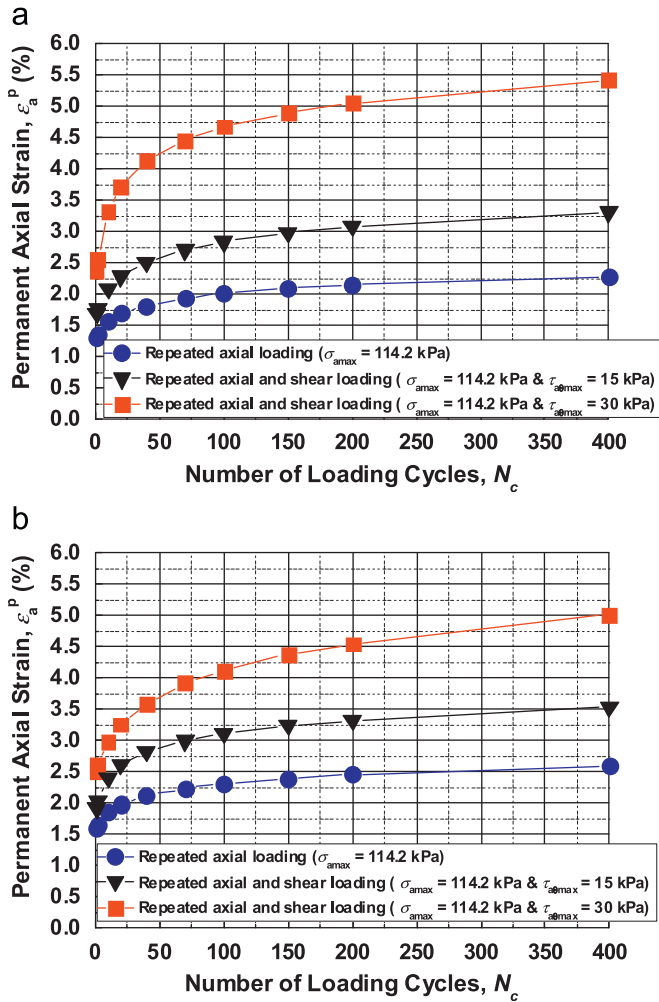


Fig. 28. Permanent deformation during cyclic loading. (a) $w=5\%$ and (b) $w=9\%$.

increases, the rotational angle of the principal stress axis also increases under the same mean principal stress. Therefore, the difference in cumulative permanent axial strain among the repeated axial loading tests, repeated axial and shear loading tests ($\tau_{a\theta\max}=15$ kPa) and ($\tau_{a\theta\max}=30$ kPa), under the same experimental conditions as shown in Fig. 28, is mainly influenced by changes in the rotational angle of the principal stress axis.

4.6. Influence of rotation of principal stress axis on cyclic plastic deformation behavior

The influence of the principal stress axis rotation has two main impacts on the deformation behavior of the unsaturated C-9.5 material in the multi-ring shear tests. One is the enhancement of the permanent axial strain of each specimen under the repeated axial and shear loading tests, as compared to the repeated axial loading tests shown in Fig. 23. The other is the shift in moisture content at the maximum cumulative permanent axial strain from the repeated axial loading tests to the repeated axial and shear loading tests.

The impact of the enhanced permanent axial strain has been discussed by many researchers. It has been found that due to the application of the shear stress, the rotation of the principal stress axis occurs, and thus, causes an increase in the axial deformation. Ishikawa et al. (2011) compared the cyclic plastic deformation results of multi-ring shear tests under cyclic loading with or without principal stress axis rotation to the results of small-scale model tests. The results of the small-scale model tests indicated similarity in the enhanced behavior of the cyclic plastic deformation in repeated axial and shear loading tests with multi-ring shear testing and examined the validity of the multi-ring shear test results. Therefore, the deformation due to the cyclic loading tests, in which the rotation of the principal stress axis is taken into account, is considered more reliable for pavement analyses, as it is closer to the phenomenon under traffic loads. In this research, the cyclic plastic deformation behavior of samples with moisture contents of 5 and 9% are compared under each cyclic loading method in order to analyze the effect of the principal stress axis rotation. These samples are selected as the maximum cumulative permanent axial strain occurs from moisture contents of 5 to 9% under each loading method. In Fig. 28, the results show that the slope of the curve for the repeated axial loading, from 200 to 400 loading cycles, is milder compared to the two other loading methods. The steepest slope of the deformation curve, from 200 to 400 loading cycles, is of the repeated axial and shear loading ($\tau_{a\theta\max}=30$ kPa). It is also noted that with an increase in the principal stress axis rotation, the stability in the particles decreases; and thus, a steeper slope is caused and the permanent axial strain increases. Therefore, cyclic loading without principal stress axis rotation shows that the slope of the curves becomes flatter and that there is more stabilization among the particles and, as a result, the permanent axial strain decreases.

The other impact of the rotation of the principal stress axis illustrates that the maximum cumulative permanent axial strain at the 400th loading cycle, under the cyclic

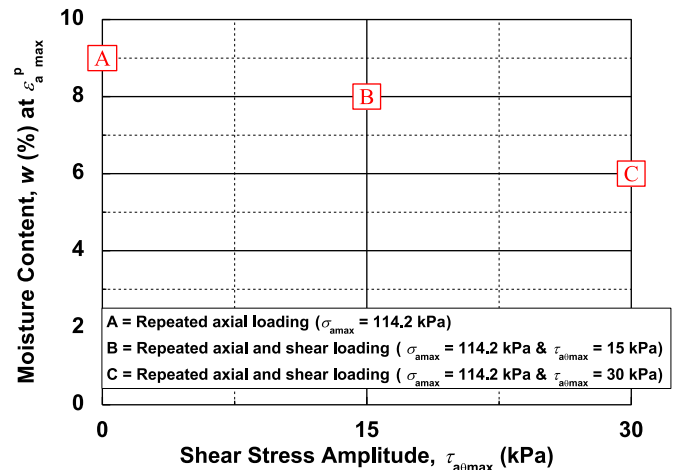


Fig. 29. Relationship of moisture content at ϵ_a^p max and shear stress amplitude at the 400th loading during cyclic loading.

loading method, occurs at a different moisture content, as shown in Fig. 29. The deformation behavior, in the repeated axial loading tests, shows that the maximum cumulative permanent axial strain occurs at the moisture content of 9%. In the case of the repeated axial and shear loading tests ($\tau_{a\theta\max}=15$ kPa), the moisture content for the maximum cumulative permanent axial strain decreases to 8%. Moreover, in the case of the repeated axial and shear loading tests ($\tau_{a\theta\max}=30$ kPa), the moisture content for the maximum cumulative permanent axial strain further decreases to 6%. It elucidates that the principal stress axis rotation increases as the shear stress amplitude increases during cyclic loading and, as a result, the moisture content associated with the maximum cumulative permanent axial strain decreases. In other words, the higher the shear stress amplitude is, the lower the moisture content value for the maximum cumulative permanent axial strain occurs. However, to support the above argument, further investigation should be carried out as future research in order to physically interpret the aforementioned phenomenon of changes in the moisture content associated with the maximum cumulative permanent axial strain under different loading methods.

5. Conclusions

On the basis of the above experimental results and discussions, the following conclusions can be obtained.

- 1) A series of static shearing tests show that there is a clear relationship among shear stress, axial strain and shear strain for unsaturated samples and indicates that the moisture content has an obvious influence on the shear behavior of granular material. Increases in the shear strain, due to the application of shear stress, causes the axial strain in unsaturated granular material to increase. This concept supports the enhanced cumulative permanent axial strain resulting from cyclic loading with principal stress axis rotation.
- 2) When the internal friction angle increases and the coefficient of earth pressure decreases, shear strength increases and axial strain decreases under constant shear strain.
- 3) The particle size distribution curves of the sample, before and after the multi-ring shear tests, infer that there is no particle breakage. This means that the moisture content does not influence the particle size distribution.
- 4) In cyclic loading tests, the rate of increase in permanent axial strain decreases with increases in the number of loading cycles, and the same phenomenon is observed under field conditions. Permanent axial strain develops mainly due to the rearrangement of the particles during cyclic loading, and the main reasons for the differences in the rearrangement or the settlement of the granular material are the moisture content and the loading method.
- 5) The influence of the moisture content under different

loading methods has some similarity, in that the increase in the moisture content reaches a certain point where maximum cumulative permanent axial strain occurs and then it gradually decreases. However, with different loading methods, the moisture content for maximum axial strain varies.

- 6) When comparing the results of the repeated axial loading tests with those of the repeated axial and shear loading tests ($\tau_{a\theta\max}=30$ kPa), the cumulative permanent axial strain obtained from the former tests is much smaller than that obtained from the latter tests. The moisture content, at the maximum cumulative permanent axial strain, shifts from 9% for the repeated axial loading tests to 6% for the repeated axial and shear loading tests ($\tau_{a\theta\max}=30$ kPa).

Acknowledgments

The authors wish to express their deepest gratitude to Mr. Hirosato Segawa, Master Course Student at Hokkaido University, for performing the water retentivity tests and arranging the experimental results.

References

- AASHTO T 307-99, 2007. Standard test method for determining the resilient modulus of soils and aggregate materials, Standard Specifications for Transportation Materials and Methods of Sampling and Testing 29th ed. (2009).
- Andrew, C.H., Juan, M.P., John, T.H., Manuel, O.B., 2004. Normalizing behavior of unsaturated granular pavement materials. *Journal of Geotechnical and Geoenvironmental Engineering* 130 (9), 896–904.
- Brown, S.F., 1996. Soil mechanics in pavement engineering. *Géotechnique* 46 (3), 383–426.
- Chan, F.W.K., Brown, S.F., 1994. Significance of principal stress rotation in pavements. In: *Proceedings of the 13th International Conference on Soil Mechanics and Foundation Engineering*. New Delhi, pp. 1823–1826.
- Fredlund, D.G., Rahardjo, H., 1993. *Soil Mechanics for Unsaturated Soil*. John Wiley & Sons, New York.
- Gräbe, P.J., Clayton, C.R.I., 2009. Effects of principal stress rotation on permanent deformation in rail track foundations. *Journal of Geotechnical and Geoenvironmental Engineering* 135 (4), 555–565.
- Ishikawa, T., Miura, S., Sekine, E., 2007. Development and performance evaluation of multi-ring shear apparatus. In: *Proceedings of the International Workshop on Geotechnical Aspects and Processed Material*. 13th September 2005, Osaka, pp. 53–64.
- Ishikawa, T., Hosoda, M., Sekine, E., Miura, S., 2008. Influence of water content on mechanical behavior of gravel under moving wheel loads. In: *Proceedings of the 1st International Conference on Transportation Geotechnics*. 25–27 August 2008, Nottingham, pp. 185–191.
- Ishikawa, T., Sekine, E., Miura, S., 2011. Cyclic deformation of granular material subjected to moving-wheel loads. *Canadian Geotechnical Journal* 48 (5), 691–703.
- Japanese Road Association, 2006. *Pavement Design Manual*. Japanese Road Association, Tokyo (in Japanese).
- Japanese Standards Association, 2009. *Test Method for Soil Compaction using a Rammer (JIS A 1210: 2009)*. Japanese Industrial Standards (in Japanese).
- Japanese Geotechnical Society, 2009. *Test Method for Water Retentivity of Soils (JGS 0151-2009)*. Japanese Geotechnical Society (in Japanese).

- Khogali, W.E.I., Elhussein, H.M., 2004. Novel approach for characterization of unbound materials. *Journal of Transportation Research Board* 1874, 38–46.
- Lekarp, F., Isacsson, U., Dawson, A., 2000a. State of the art. I: Resilient response of unbound aggregates. *Journal of Transportation Engineering* 126 (1), 66–75.
- Lekarp, F., Isacsson, U., Dawson, A., 2000b. State of the art. II: Permanent strain response of unbound aggregates. *Journal of Transportation Engineering* 126 (1), 76–83.
- Lu, N., Likos, W.J., 2004. *Unsaturated Soil Mechanics*. John Wiley and Sons Inc., New Jersey, Hoboken.
- Maina, J.W., Matsui, K., 2004. Developing software for elastic analysis of pavement structure responses to vertical and horizontal surface loadings. *Journal of the Transportation Research Board* 1896, 107–118.
- Miura, K., Miura, S., Toki, S., 1986. Deformation behavior of anisotropic dense sand under principal stress axis rotation. *Journal of Soils and Foundations* 26 (1), 36–52.
- Powrie, W., Yang, L.A., Clayton, C.R.I., 2007. Stress changes in the ground below ballasted railway track during train passage. *Proceedings of the Institution of Mechanical Engineers, Part F: Journal of Rail and Rapid Transit* 221 (2), 247–262.
- Vanpalli, S.K., Fredlund, D.G., 1999. Empirical procedures to predict the shear strength of unsaturated soils. In: *Proceedings of the 11th Asian Regional Conference on Soil Mechanics and Geotechnical Engineering*. 16–20 August 1999, Seoul, pp. 93–96.